QUAX Activity Report 2023

D. Alesini, D. Babusci, M. Beatrici (Tecn.), A. Calanca (Tecn.), A. D'Elia (AR), D. Di Bari (Tecn.), D. Di Gioacchino, C. Gatti (Resp.), S. Lauciani (Tecn.), C. Ligi, G. Maccarrone, D. Moricciani, G. Papalino (Tecn.), G. Pileggi (Tecn.), A. Rettaroli (AR), S. Tocci (TD), G. Vidali (Laur.)

1 First search for galactic axions with the QUAX-LNF haloscope

We report on the first operation of the new QUAX haloscope located at LNF, which doubles the search potential of the QUAX experiment along with the LNL haloscope.

The first data-taking was performed in December 2023, and additional details can be found in the preprint arXiv 2402.19063.

1.1 Haloscope description

The haloscope, schematized in Fig. 1, consists of a cylindrical OFHC copper resonant cavity, with inner radius $r = 13.51$ mm and height $h = 246$ mm, for a total volume $V = 0.141$ l. Two coaxial cables are coupled to the cavity via dipole antennas. One antenna is fixed and weakly coupled, with coupling estimated from simulations 1.4×10^{-3}, the other is connected to a linear stepper motor whose movement allows the tunability of the coupling β.

The magnetic field is provided by a NbTi superconducting solenoid magnet with a cold bore diameter of 100 mm and 320 mm height. On top of the magnet, a second coil assures the reduction of the stray field above the cavity below few hundred Gauss. The magnet, initially operated at the nominal field of 9 T, was set to a lower safety value following a quench during a current ramp. The experiment here described was then conducted at 8 T, with a field inside the cavity volume of r.m.s. $\sqrt{\langle B_0^2 \rangle} = 6.73$ T. As amplification stages, line 5 is provided with a cryogenic HEMT (at 4 K) and a FET.

The setup is hosted in a Leiden Cryogenics CF-CS110-1000 dilution refrigerator equipped with two Sumitomo pulse tubes of 1.5 W at 4 K each. The refrigerator is segmented in different temperature stages. The magnet and the HEMT are thermalized at the 4 K stage, while the cavity is connected to the last temperature stage which attained 20 mK at equilibrium. The cavity temperature, monitored during the data taking, reached about 30 mK.

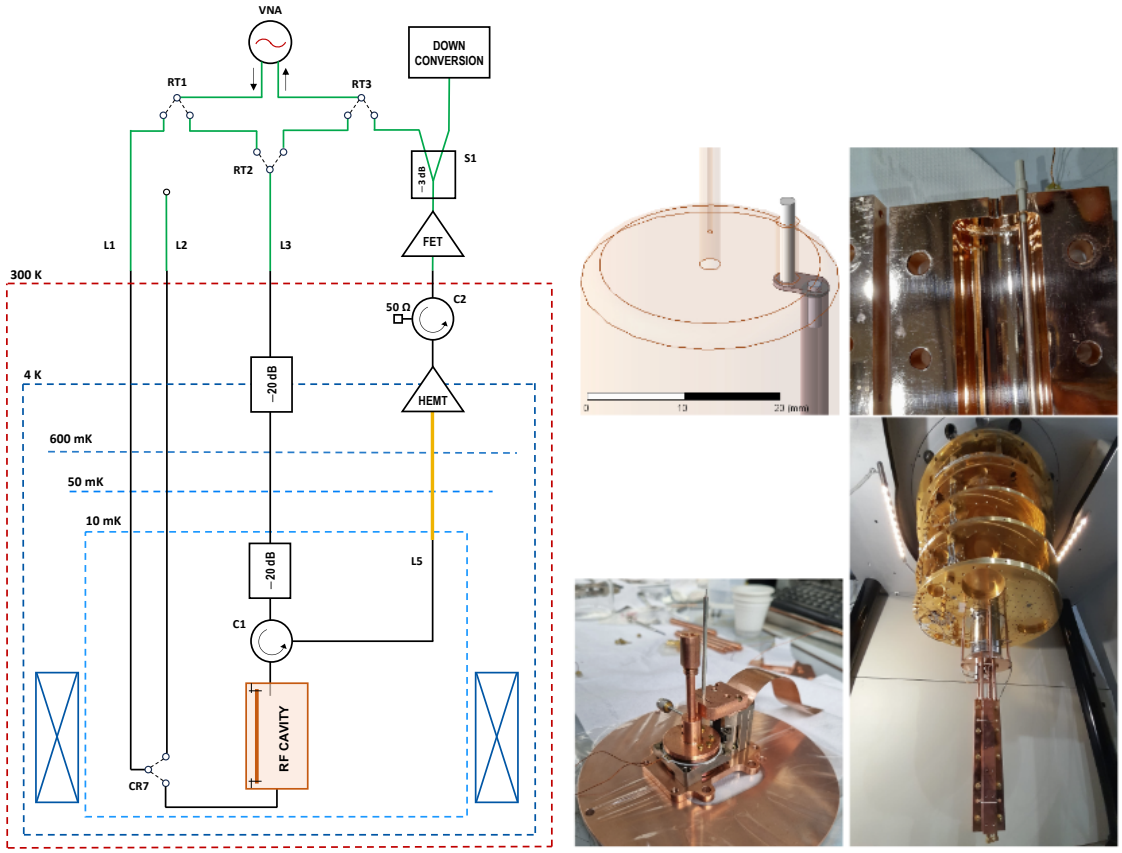

Figure 1: Left) *Experimental setup sketch. The successive temperature stages of the dilution refrigerator are shown with their base temperature. L1 and L3 are input RF lines, L5 is the output amplified line and L2 is an auxiliary line used for further checks. Note that L1, L2 and L3 have intrinsic attenuations of about 15 dB each. The room temperature switches (RT1, RT2, RT3) and the cryogenic switch (CR7) allow all the combinations required for measurements and calibrations. Attenuators are indicated with their attenuation values, while C1 and C2 are circulators. A superconductive RF cable in L5 is indicated in yellow. The magnet is shown as two crossed squares and is thermalized in the 4 K vessel. The HEMT and FET are, respectively, the cryogenic and room-temperature amplifiers, whereas the power splitter is indicated as S1.* Right) *In order, detail of the rod tuning mechanism design as seen in the simulator, picture of one end of the rod with the PEEK support, the two stepper motors detail, view of the assembled haloscope.*

1.2 Frequency tuning

The frequency tuning is obtained by moving a copper rod with radius 1.5 mm and length 244 mm inside the cavity volume (Fig. 1 right). The effective cavity volume is then reduced to $V = 0.139$ l. The rod is supported by PEEK nails, which are centered off-axis with respect to the rod, as shown in Fig. 1 right. At one end, the PEEK is grabbed by a copper mandrel, which is rotated by the stepper motor. Thanks to this movement, the rod accomplishes an arc of circumference approaching the center of the cavity. The electromagnetic behavior of this system was simulated with the ANSYS HFSS suite. The resonant mode of interest, TM010, has a starting frequency of 8.817 GHz when the (ideal) rod is at rest in contact with the cavity wall. Moving the rod towards the center, the mode is squeezed and simulations indicate that the frequency is tuned up to 9.106 GHz with a rotation of 80 degrees, while keeping the geometric factor C_{010} close to its ideal value and with a reduction of the quality factor of about 10%.

The rod orientation is changed by a rotative stepper piezoelectric motor from Attocube Systems model ANR240, while the second linear motor, as anticipated, moves the tunable antenna (model ANPz111). Both motors were operated at cryogenic temperatures, between 20 and 30 mK, without complications, and with a heating up of the environment of only a few mK when operated in single-step mode.

The measured value of the quality factor was $Q_0 \simeq 50000$ and the coupling was kept at $\beta = 0.5$.

1.3 Data taking

After the cool-down, the following procedure is used for calibrating and taking data at each frequency step, starting from the first measured value of 8.8317690 GHz.

- The cavity frequency is set moving the ANR240 motor step by step while monitoring the S_{51} from the VNA. Each time the frequency is increased by one cavity bandwidth, about 260 kHz, with respect to the previous data taking.
- The waveforms of the scattering parameters S_{51}, S_{53} and S_{13}, named according to the line numbering in Fig. 1, are collected with the VNA, to perform the calibration.
- The raw data acquisition is started, lasting about 3600 s.

The data acquisition consists in recording the power coming from the output line L5. With an I–Q mixer we convert the frequency to the baseband, and the I and Q quadratures are amplified by low-noise voltage amplifiers ($\times 10^3$ factor, 10 MHz bandwidth) before being digitized by a 16-bit ADC board, which has a 2 MHz bandwidth and sampling of 2 MS/s. In each sub-run, the I and Q signals are acquired for 4 seconds and saved to file. The total amount of files in each sub-run is 941, resulting in an integration time of $\Delta t = 3764$ s.

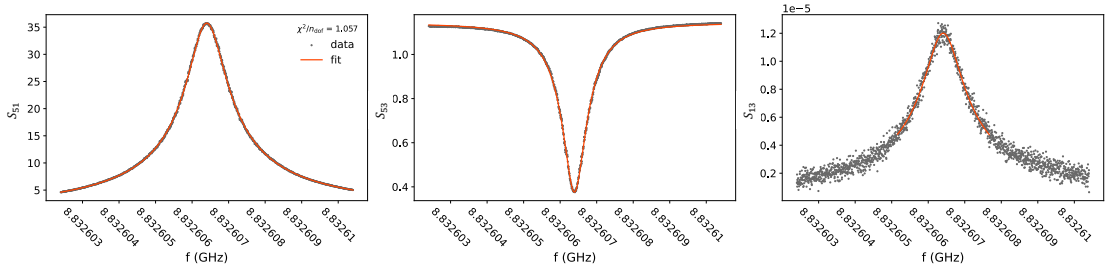

Figure 2: *Fit example of the scattering parameters S51 (forward transmission), S53 (reflection) and S13 (backward transmission) to extract the cavity parameters and gain in the calibration.*

The calibration procedure is done by a simultaneous fit of the S_{51}, S_{53} and S_{13} spectra with their analytical expressions, allowing the extraction of the cavity parameters ν_c, Q_0, β and of the attenuation and gain of the input and output lines (see Fig. 2). In particular, we are interested in the gain of Line 5, which is calculated solving a system of three coupled equations:

$$\begin{aligned} S_{51} &= L1 + s_{21}^{\mathrm{cav}}(\nu_c, Q_0, \beta) + L5, \\ S_{53} &= L3 + s_{22}^{\mathrm{cav}}(\nu_c, Q_0, \beta) + L5, \\ S_{13} &= L1 + s_{12}^{\mathrm{cav}}(\nu_c, Q_0, \beta) + L3, \end{aligned} \tag{1}$$

where s_{ij}^{cav} are the intrinsic transmission and reflection coefficients of the resonant cavity, having Lorentzian shape. The measured gain is $G_5 \approx 70.0$ dB through all the sub-runs, with a systematic uncertainty of 0.4 dB. Separately, the gain and the spectrum shape from the splitter output to the ADC are measured, taking into account the effect of the ADC internal filters.

1.4 Data analysis and results

The cavity resonance frequency ν_c is tuned in a 6 MHz range between 8.831769–8.8377664 GHz in 24 steps, as shown in Fig. 3. For each dataset we calculate the power spectrum by combining the quadratures as $I - iQ$, computing the FFT and taking the squared module. The spectra are centered at the LO frequency, which is always $\nu_{\mathrm{LO}} = \nu_c - 500$ kHz, and are corrected for the Line 5 gain G_5 and for the spectrum shape of the downconversion electronics.

For each frequency step, we estimate T_{sys} from the output power, properly converted into units of Kelvin, at a reference frequency ν_{LO}+100 kHz, where 1/f noise is negligible and still far enough from the cavity resonance, obtaining an average value of 4.7 K. We calculate the power spectrum residuals by subtracting it to a polynomial obtained with a Savitzky-Golay (SG) filter from the spectrum itself, in a window of about 530 kHz centered a ν_c. The normalized residuals follow a Gaussian distribution, with a standard deviation compatible with 1.

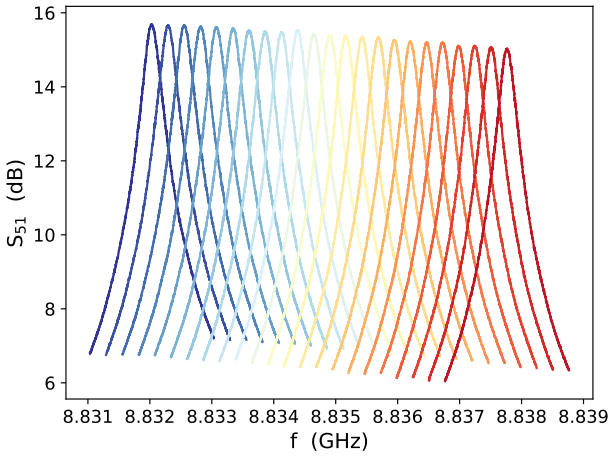

Figure 3: *Transmission spectra (S51) of the haloscope cavity for different resonant frequencies. We tuned the resonance of the cavity in the 6 MHz frequency window during the axion search.*

For each axion mass, we adopt a standard analysis procedure used in this field, consisting in calculating the Maximum Likelihood of the difference between the normalized residuals and the signal model expected for axions. From this, the estimated value of the coupling constant $g_{a\gamma\gamma}$ for each value of axion mass in the range $36.5241 - 36.5510$ μeV was interpreted as exclusion limit. The efficiency of the SG filter is estimated by performing Monte Carlo simulations injecting a fake axion signal into the power spectra with known coupling constant. The comparison between $g^2_{\rm calculated}$ and $g^2_{\rm injected}$ gives an efficiency of 0.845.

In Fig. 4 we show the upper limit $g^{\rm CL}_{a\gamma\gamma}$ in an axion mass window of 27.02 neV centered around 36.53764 μeV. The maximum sensitivity obtained with a 90% CL is $g^{\rm CL}_{a\gamma\gamma} < 0.861 \times 10^{-13}$ GeV^{-1}. This value is about 5 times larger with respect to the benchmark QCD axion level of the KSVZ theory.

2 List of Conference Talks by LNF Authors in Year 2023

1. A. Rettaroli, *Haloscopes*, Kick-off meeting of COST action Cosmic Whispers (CA21106), INFN-LNF, Frascati – Feb 2023

2. A. Rettaroli, *Towards quantum detection of axions in the QUAX experiment*, Dark Matter 2023, Santander (Spain) - May 2023

3. A. Rettaroli, (poster) *Design, fabrication and characterization of a ultra-high-Q resilient Nb3Sn resonant cavity*, Quantum Technologies for Fundamental Physics, EMFCSC, Erice - Sept 2023

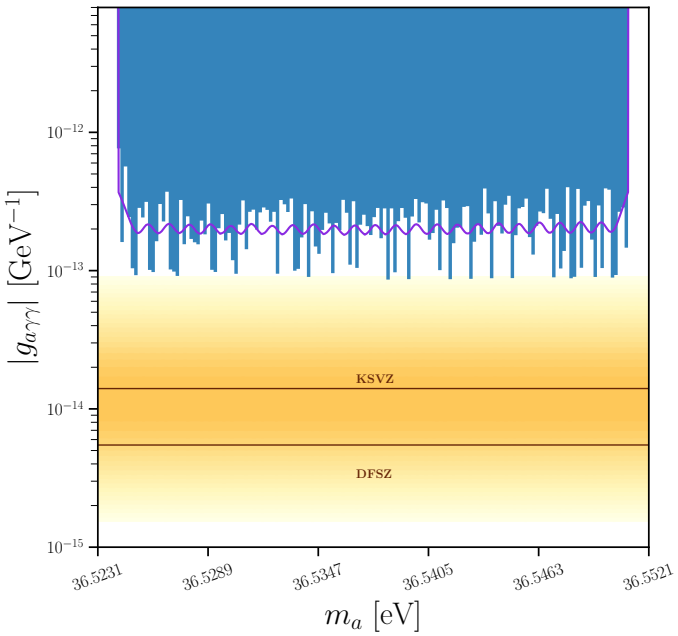

Figure 4: *The 90% single-sided C.L. upper limit for $g_{a\gamma\gamma}$ as a function of the axion mass. The blue solid curve represents the expected limit in the case of no signal. The yellow region indicates the QCD axion model band.*

4. C. Gatti, *Search for Axion Dark Matter*, Seminar at La Sapienza university, Rome - March 2023

5. C. Gatti, *The Axion Program of QUAX and FLASH*, Axions across boundaries between Particle Physics, Astrophysics, Cosmology and forefront Detection Technologies, The Galileo Galilei Institute For Theoretical Physics, Arcetri - June 2023

6. C. Gatti, *Axion Research Program at LNF*, 18th Patras Workshop on Axions, WIMPs and WISPs, Rijeka - July 2023

7. C. Gatti, *Recent QUAX results on axion searches and prospects for the FLASH experiment*, 3rd IBS Conference on Dark World 2023, ISC Science Culture Center, Dajeon (South Korea) - October 2023

3 Publications

- R. Di Vora et al., *Search for galactic axions with a traveling wave parametric amplifier*, Phys. Rev. **108**, 062005 (2023), DOI: 10.1103/PhysRevD.108.062005

- A. Rettaroli et al., *Search for Axion dark matter with the QUAX-LNF tunable haloscope*, (preprint) arXiv 2402.19063, https://arxiv.org/abs/2402.19063
- D. Alesini et al., *The future search for low-frequency axions and new physics with the FLASH resonant cavity experiment at Frascati National Laboratories*, Phys. Dark Univ. **42**, 101370 (2023)

4 Acknowledgements

Partially supported by EU through FET Open SUPERGALAX project, grant agreement N.863313.